POLITECNICO DI TORINO

Department of Mechanical and Aerospace engineering

Master's Degree in Aerospace Engineering

Master's Degree Thesis

escape and interplanetary trajectory optimization from Earth-Moon L2

Supervisor:
Prof. Lorenzo Casalino

Candidate:
Elisa Raduazzo

ACCADEMIC YEAR 2021/2022

Abstract

This thesis is about trajectory optimization for missions towards asteroids and departure from Lagrangian points, by means of an indirect method, based on optimal control theory.

Space exploration is constantly increasing and Lagrangian points proved to be strategic locations for either unmanned scientific missions or human outposts, thanks to the natural stabilization created by the balance of gravitational and centripetal forces. The study of optimal trajectories is therefore becoming increasingly necessary.

A medium-size spacecraft was considered in the present study, whose final objective is to maximize final mass of the spacecraft, thus reducing fuel consumption as much as possible. 4-body gravitational influence with Solar Radiation Pressure (SRP) as perturbation, is considered as dynamic model. JPL ephemeris were used to track celestial body positions. The spacecraft is seen as a variable mass point. EME2000 is adopted as reference frame. Optimization code exploits Pontryagin's Maximum Principle (PMP) and basically solve a Boundary Values Problem (BVP): a solution compliant with external constraints is sought perturbing the initial solution and adjusting values after error evaluation. The method results to be very sensitive to trial solution used, enough to compromise convergence if not scrupulously chosen.

A mission towards Near Earth Asteroids (NEA) (specifically asteroid 2016 TB57) was investigated in the study, analysing departure dates during October and November 2025. Trajectory was divided into 2 parts: escape trajectory departing from Earth-Moon Lagrangian Point 2 (EML2) (in a Geocentric reference frame) and interplanetary arc (studied in a Heliocentric reference frame). Considering one-week apart starting times (during one Moon synodic period around

Earth) and alternately imposing final time or final energy as constraints, optimum was manually detected. Escapes were initially sought as 2-phase (single burn), but 4-phase (2 burns) approach was also used when needed in order to maximize final mass.

The results showed that departure date, thus initial position of the spacecraft with respect to the Sun, could have an influence on fuel consumption whether Sun perturbation acts in a positive or negative way. Two families of solution were found; optimal trajectory happened to belong to the second family of solutions, escaping Earth SOI in the fourth quadrant (considering equatorial plane in a Geocentric reference frame). As far as interplanetary trajectory is concerned, a local optimum appeared among the initial times considered, on the 15^{th} October 2025, having the lowest fuel consumption.

Further studies should consider more departure dates in order to detect the optimum in a more precise way; different asteroids should also be taken into account.

Contents

1 Earth-Moon-Sun system **3**

1.1 Earth-Moon . . . 3

1.1.1 Center of mass . . . 3

1.1.2 Orbital parameter and their perturbations . . . 4

1.1.3 Lunar librations . . . 5

1.2 Lagrangian points . . . 6

1.2.1 Lagrangian points definition and characteristics . . . 6

1.2.2 Circular restricted 3-body problem in the Earth-Moon system 6

1.2.3 Potential function . . . 9

1.2.4 Derivation from potential equation . . . 10

1.2.5 Jacobi's integral . . . 12

1.3 Interplanetary trajectories . . . 14

2 Optimization method **16**

2.1 Indirect method . . . 16

2.2 Optimal Control Theory (OCT) . . . 17

2.2.1 Theoretical approach . . . 17

2.2.2 Application to the case study . . . 19

2.3 Boundary Values Problem (BVP) . . . 20

2.3.1 Formulation of the problem . . . 21

2.3.2 Numerical solution . . . 21

2.4 Code structure . . . 22

2.4.1 User interface . . . 22

2.4.2 Structure and subroutines . . . 23

3 Dynamic model **25**
3.1 Reference frames . . . 25
3.1.1 EME2000 . . . 25
3.1.2 Equations of motion . . . 27
3.2 State equations . . . 28
3.3 Perturbations . . . 29
3.3.1 Earth Potential Model . . . 30
3.3.2 Lunisolar Perturbation . . . 31
3.3.3 Solar Radiation Pressure (SRP) . . . 32

4 Procedure and results **33**
4.1 Definition of the case study mission . . . 33
4.2 Escape from EML2 . . . 34
4.2.1 Escape with constrained duration . . . 35
4.2.2 Escape with constrained final energy . . . 39
4.2.3 Optimal escape trajectory analysis . . . 41
4.3 Trajectory towards 2016 TB57 . . . 43
4.3.1 Global evaluation . . . 43
4.3.2 Optimal interplanetary trajectory . . . 47

5 Conclusions **49**

List of Figures

1.1 Earth-Moon mass center visualization (not in scale) 4
1.2 Earth-Moon rotating reference frame representation (not in scale) . 7
1.3 Graphical representation of the five Lagrangian point and their distance from Earth and Moon, expressed in terms of Earth-Moon distance R. Source: Ref [8] 11
1.4 Intersection of the zero-velocity surfaces with xy plane for various values of C. Source: Ref [13] 13

3.1 EME2000 and topocentric reference frame 25
3.2 Geoid height, computed from the gravity field model EGM2008(Pavlis et al., 2012). Source: Ref [2] 30

4.1 graphical display of the amount of fuel consumed to escape having a constraint in duration Dt 37
4.2 Representation of Sun, Earth and Moon relative positions (not in scale) 38
4.3 Graphical display of the amount of fuel consumed to escape having a constraint in c3 40
4.4 Graphical display of the amount of fuel consumed to escape 41
4.5 Optimal Escape trajectories and detail of initial positions 42
4.6 Graphical display of the amount of fuel consumed in the interplanetary maneuver to Asteroid 2016 TB57. 44
4.7 Semi-major axis variation during time for interplanetary trajectories, compared with c_3 development 45

4.8 Peri-apsis (a) and apo-apsis (b) development during interplanetary trajectories 46
4.9 Energy and switching function comparison during time 48

List of Tables

1.1 Potential $\mathcal{U}$ and Jacobi's constant C values for Lagrangian Points . 13

4.1 Time conversion at initial point of the maneuver 34
4.2 Fuel Consumption for escape missions with constrained Dt and free c3 36
4.3 Moon angle $\theta_{☾}$ at departure time in EML2 37
4.4 Fuel Consumption for missions with constrained final energy $c_3 = 0.3$ 40
4.5 Cases selected as local optimal for escape trajectories 42
4.6 Case selected as optimal for interplanetary trajectories 44
4.7 Position and velocity components in heliocentric reference frame at the end of escape 46
4.8 Orbital parameters at the end of escape. 47

Acronyms

AU Astronomic Unit

BVP Boundary Values Problem

EGM2008 Earth Gravitational Model 2008

EME2000 Earth Mean Equator and Equinox of Epoch J2000

EML2 Earth-Moon Lagrangian Point 2

ESA European Space Agency

IVP Initial Value Problem

NEA Near Earth Asteroids

NRHO Near-Rectilinear Halo Orbit

OCT Optimal Control Theory

PMP Pontryagin's Maximum Principle

SF Switching Function

SOI Sphere of Influence

SRP Solar Radiation Pressure

Introduction

For the last two decades, asteroids have increasingly been chosen as destinations for deep space exploration missions; firstly with the aim to investigate chemical composition of the surface, more recently as target for planetary defence demonstrations. The first actual mission towards a Near Earth asteroid was in 1996 when NEAR Shoemaker (Near Earth Asteroids Randezvous), was launched from Cape Canaveral. NEAR was designed to reach Eros and collect data and images from a close orbit, in order to understand its characteristics. Since then, many other missions were lead by major space agencies, involving asteroids as part or main purpose of the mission. Amongst the most famous worth mentioning: Deep Space 1 (DS1) a probe performing a fly by on the Near-Earth asteroid 9969 Braille (formerly known as 1992 KD); Hayabusa (formerly Muses-C) in 2003 and Hayabusa2 (2014) the Japanese missions whose objective is primarily to collect and return a sample of material respectively from the small asteroid 25143 Itokawa (1998 SF36) and from Ryugu; Dawn (2007), the NASA orbiter of Ceres and Vesta and the recent DART (Double Asteroid Redirection Test) mission: the first interplanetary defence mission which aims to demonstrate the concept of the trajectory deviation, protecting Earth from a potentially hazardous impact [10].

The open question in early phase of mission design always concerns the optimal trajectory necessary to reach the desired arrival point in space. Lagrangian points (or Libration point) revealed good starting positions for these types of mission [5]. They are unstable equilibrium points in binary systems, therefore a tiny amount of ΔV (thus fuel) is needed in order to escape from the system Sphere of Influence (SOI) and the cost of the mission is easily lowered. Moreover, gravitational and centrifugal forces are balanced, so that the probe can stay in a sort of waiting orbit around this particular point, where a good stability is guaranteed just with minimal thruster corrections for station keeping maneuver. The area around these points in space has other interesting properties for a variety of missions. For example there are missions like Planck, which maps relic radiations, trying to demonstrate theories on the evolution of the universe and Gaia, which makes a survey of the stars in our galaxy. Also the brand new James Webb Telescope is orbiting the second Lagrangian point in Sun-Earth binary system and it's provided with a large Sun-shield designed to block light and heat from Sun, Earth and Moon, preventing interference with the optic payload on the cold side.

As far as Earth-Moon system is concerned, cooperation of NASA, ESA, CSA and JAXA led to a great international project called Deep Space Gateway: the next human outpost orbiting around the Moon, which could be used as final or intermediate way-point for the future human exploration missions towards Moon and Mars. The space station will move on a Near-Rectilinear Halo Orbit (NRHO) around Earth-Moon Lagrangian Point 2 (EML2), with a 7-day period. This orbit is highly eccentric in order to guarantee passages nearby lunar surface as well as orbit arcs closer to Earth, so that journey isn't too expensive in terms of both time and fuel or money expenses. It's clear that this specific type of orbit, which draws a sort of halo around the celestial body, has also been selected because the spacecraft remains always visible from Earth: this is crucial for real time communications [5].

In this thesis a mission towards asteroid 2016 TB57 with departure point in EML2 was investigated. More specifically, the use of an indirect optimization method was studied. Implementing the method, the trajectory was divided into 2 segment: a geocentric phase (escape from Earth SOI) and an interplanetary one (using heliocentric reference frame). The aim was to optimize the final mass, thus minimize the fuel consumption for the mission. In the first chapter main features of the Earth-Moon system will be pointed out. In the following chapters optimization method will be explained, then dynamic system and reference frames will be defined. Finally results will be presented and analyzed.

Chapter 1

Earth-Moon-Sun system

1.1 The Earth-Moon system main features

Earth-Moon system is interesting to study, not only because it directly affect us in everyday life or for the presence of two celestial bodies orbiting around one center of attraction. It's the scale of the two masses in the system to be unique: Moon mass is about 1/80th the mass of Earth, which is a much larger ratio, compared with every other binary system in the solar system. Its features can be considered very similar to a double planet,that's because "arise several irregularities in her motion", as Sir Newtons wrote about the Moon in Book I of the *Principia* [1, p. 321].

1.1.1 Center of mass

One first important notion worth to mention is that Earth and Moon revolve about the whole system center of mass, meanwhile it revolves around the Sun. The mean distance between the center of mass of Earth and the center of mass of the Moon is 384400 km. Knowing this datum and the values of the gravitational constants of the two bodies ($\mu_{☾} = 4904 \quad km^3/s^2$ for Moon and $\mu_{♁} = 398000 \quad km^3/s^2$ for Earth) it's easy to derive the position of the Earth-Moon system center of mass, through a simple proportion.

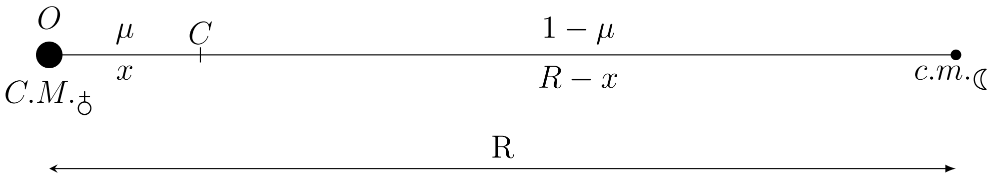

Figure 1.1: Earth-Moon mass center visualization (not in scale)

$$OC = \frac{\mu_{\text{☾}} \cdot R}{\mu_{\text{♁}} + \mu_{\text{☾}}} = \frac{R}{\frac{\mu_{\text{♁}}}{\mu_{\text{☾}}} + 1} = 4671\,km \tag{1.1}$$

It is obtained that the binary system center of mass is 4671 km away from Earth center of mass, at about 3/4th of the planet radius. For the sake of preciseness, should be noted that the center of mass of the system arise from the Earth-Moon conjunction line because of the tidal bulge caused by the oceans. The *tidal coupling* is responsible for the increase of the distance between the two bodies: oceans rotates with Earth creating a friction which slows down Earth angular velocity, shortening terrestrial rotation by the amount of 1.46 ms per century.

1.1.2 Orbital parameter and their perturbations

Moon orbit viewed with respect to Earth, can be described by the classical orbital parameters, but the presence of the gravitational force of the Sun, causes a continuous variation in their values. The main perturbations are listed below:

- Semi-major axis a has a 5% variation from the average, with a minimum of 363300 km to a maximum of 405500 km (with an average value of 384400 km as mentioned before).

- "Draconic period" T (i.e. the time taken for a complete revolution of Moon around Earth) is 27.3166 hour long on average, with a variation of 7 hours. It is equal the revolution period of the Moon about its axis, that's why from Earth we are able to see always the same side of the Moon.

- Eccentricity e is 0.059 on average, oscillating from 0.044 to 0.067. This is called the "*evection*" effect and it has a period of 31.8 days.

- The line of nodes (i.e. intersection of Moon orbital plane and the ecliptic) is subjected to the phenomenon of precession, rotating westward with a period of 18.6 years and causing a decrease of RAAN parameter Ω (Right ascension of ascending node).

- Inclination i (defined as the angle between the planes containing Moon equators and the ecliptic) changes during time, from a minimum of $4°59'$, to a maximum of $5°18'$ (the average value is $5°9'$). Considering the inclination of Earth's equator with respect to the ecliptic ($23°27'$), variations are between a minimum of $18°19'$ when the descending node of the Moon's orbit coincides with the vernal equinox, and a maximum of $28°35'$, when ascending node is at the vernal equinox.

- The line of apsides (i.e. the line joining apogee and perigee) also have a precession of about $3°/rev$. This results in a variation in the peri-apsis argument ω, which completes a full revolution every 8.9 years.

1.1.3 Lunar librations

There is another type of perturbation: the Lunar libration, also called "rocking motion", thanks to which it's possible to observe more than exactly 50% of the surface. It is due to two different causes: a geometrical one and a physical one.

- *Geometrical Librations in longitude* are caused by the fact that the Moon increases its velocity around perigee and slows down near apogee, while angular velocity around its axis is constant. This makes visible about 7.75° more around the day-night line.

- *Geometrical Librations in latitude* is due to the tilt of the Moon's rotation axis of 6.5° that allows to see part of the surface beyond the poles, alternating every half revolution.

- *Physical Librations* are due to the gyroscopic effect: the long diameter of both Earth and Moon tend to align with the line joining the centers of mass, this causes little daily oscillation. Also the tidal effect can be considered as a cause of this perturbation

1.2 Lagrangian points

1.2.1 Lagrangian points definition and characteristics

Binary systems are matters of interest because of properties they have in special locations: the so called Lagrangian points. Lagrangian points are particular locations in a binary system, where gravitational forces of two masses equal the centripetal force of a small satellite orbiting with them, creating an equilibrium point where a satellite is not subjected to any acceleration relative to the rotating frame. The spacecraft is ideally stationary, therefore fuel consumption around these particular positions in space is reduced, this makes them an interesting arriving point for several observing missions where stationarity is required (James Webb Telescope is an example) as well as departure point in exploration missions.

1.2.2 Circular restricted 3-body problem in the Earth-Moon system

In order to better understand a satellite motion near a Lagrangian point, a simpler model is now taken into account: the restricted 3 body problem. Only gravitational forces coming from two celestial bodies having a much greater mass than the third one will be considered, neglecting any additional body; orbits will be assumed as circular, hence with null eccentricity. The two massive bodies will be denoted with m_1 and m_2, where $m_1 > m_2$, the third small body can be imagined as an artificial satellite having no gravitational influence on m_1 or m_2, it will be denoted with m. In order to simplify notation, let's define the cumulative gravitational coefficient $\mu = \dfrac{m_2}{M}$ where $M = m_1 + m_2$. Now the two masses can be written only in terms of the total mass of the system M and the ratio between the two massive bodies μ:

$$m_2 = \mu M \qquad m_1 = (1 - \mu)M.$$

The center of mass position can be calculated with a proportion and will result at a distance amounting to μR from m_1 as represented in figure 1.2, where R is the distance between m_1 and m_2.

A reference frame should also be defined,A rotating reference frame with an-

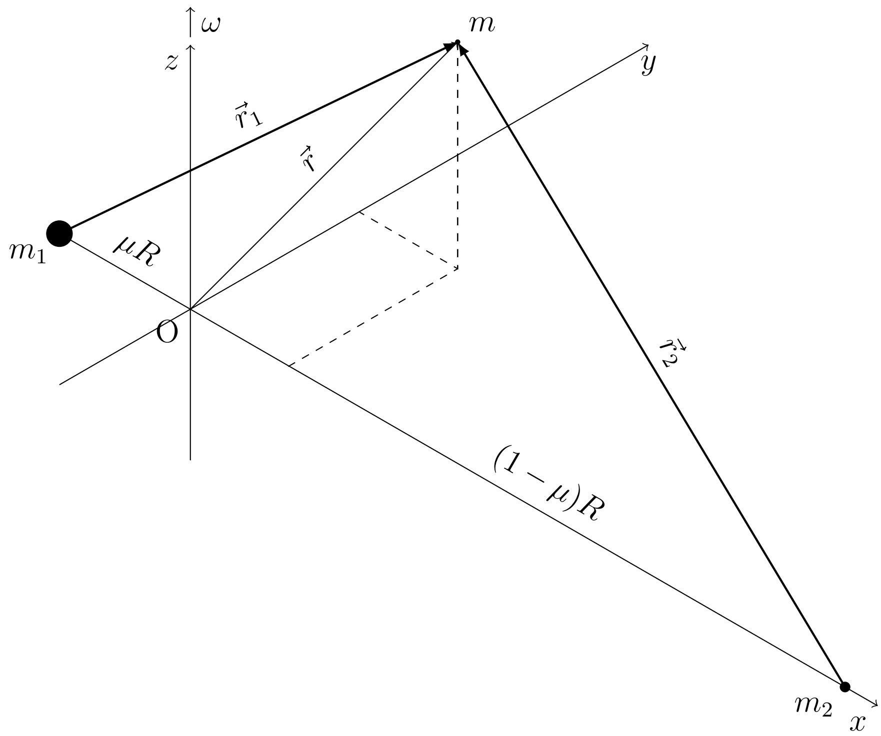

Figure 1.2: Earth-Moon rotating reference frame representation (not in scale)

gular velocity $\boldsymbol{\omega}$ is defined: it has his origin at the center of mass of the system; x-axis lying on the line joining m_1 and m_2; it considers as fundamental plane xy the plane of motion, so where m_1 and m_2 orbits lie. Positions of the masses and forces among them is displayed in figure 1.2 and written as vectors as follows:

$$\mathbf{m_1} = \begin{Bmatrix} -\mu R \\ 0 \\ 0 \end{Bmatrix} \qquad \mathbf{m_2} = \begin{Bmatrix} (1-\mu)R \\ 0 \\ 0 \end{Bmatrix} \qquad \mathbf{m} = \vec{r} = \begin{Bmatrix} x \\ y \\ z \end{Bmatrix}$$

are the position of the three masses in the reference frame and

$$\vec{r}_1 = \begin{Bmatrix} x+\mu R \\ y \\ z \end{Bmatrix} \qquad \vec{r}_2 = \begin{Bmatrix} x-(1-\mu)R \\ y \\ z \end{Bmatrix}$$

are the position vectors of m seen respectively from m_1 and m_2.

At this point, equation of motion for m with respect to the system center of mass will be derived, remembering that the reference framer is not inertial, hence centripetal and Coriolis acceleration must be taken into account. From the Newton's second law for the mass m:

$$\bar{a} = \frac{\bar{F}}{m}.$$

Values of our interest are substituted:

$$\boldsymbol{\ddot{\vec{r}} + \omega \wedge (\omega \wedge \vec{r}) + 2\omega \wedge \dot{\vec{r}} = \frac{1}{m}(\bar{F}_1 + \bar{F}_2)} \tag{1.2}$$

where every term in the equation should be spelled out in order to ease following calculations:

- $\bar{F}_1 = -G \cdot \frac{m_1 m}{\bar{r}_1^2} \frac{\bar{r}_1}{|\bar{r}_1|} = -G \cdot m \cdot \frac{(1-\mu)M}{\bar{r}_1^3} \bar{r}_1;$
- $\bar{F}_2 = -G \cdot \frac{m_2 m}{\bar{r}_2^2} \frac{\bar{r}_2}{|\bar{r}_2|} = -G \cdot m \cdot \frac{\mu M}{\bar{r}_2^3} \bar{r}_2$ by Newton's Law of universal gravitation;
- $\omega \wedge \vec{r} = \begin{vmatrix} \hat{i} & \hat{j} & \hat{k} \\ 0 & 0 & \omega \\ x & y & z \end{vmatrix} = \tilde{\boldsymbol{\omega}} \begin{Bmatrix} x \\ y \\ z \end{Bmatrix} = \begin{bmatrix} 0 & -\omega & 0 \\ \omega & 0 & 0 \\ 0 & 0 & 0 \end{bmatrix} \begin{Bmatrix} x \\ y \\ z \end{Bmatrix} = \begin{Bmatrix} -\omega y \\ \omega x \\ 0 \end{Bmatrix}$ by definition of cross product;
- $\boldsymbol{\omega} \wedge (\boldsymbol{\omega} \wedge \vec{r}) = \begin{Bmatrix} -\omega^2 x \\ -\omega^2 y \\ 0 \end{Bmatrix}$ following the same steps above;
- $2\boldsymbol{\omega} \wedge \dot{\vec{r}} = \begin{Bmatrix} -2\omega \dot{y} \\ -2\omega \dot{x} \\ 0 \end{Bmatrix}$ considering that $\dot{\vec{r}} = \begin{Bmatrix} \dot{x} \\ \dot{y} \\ \dot{z} \end{Bmatrix}$.

Manipulating and separating into three components along the reference frame axis, equation of motion system below will be obtained:

$$\begin{cases} \ddot{x} - \omega^2 x - 2\omega\dot{y} = -G \cdot M\dfrac{1-\mu}{r_1^3}(x+\mu R) - G \cdot M\dfrac{\mu}{r_2^3}[x-(1-\mu)R] \\ \ddot{y} - \omega^2 y + 2\omega\dot{x} = -G \cdot M\dfrac{1-\mu}{r_1^3} \cdot y - G \cdot M\dfrac{\mu}{r_2^3} \cdot y \\ \ddot{z} = -G \cdot M\dfrac{1-\mu}{r_1^3} \cdot z - G \cdot M\dfrac{\mu}{r_2^3} \cdot z \end{cases} \tag{1.3}$$

Solution in terms of position can be obtained by integration, keeping in mind that equations are non linear, hence the process will be iterative. Furthermore the choice of initial condition will affect the results, forcing us to proceed by trial and error.

1.2.3 Potential function

Despite the complexity of the problem, a deeper study of space around Earth and Moon can be made through the potential function. Its gradient which in the case of three-body problem, is defined as

$$U = -G\left(\frac{m_1}{r_1} + \frac{m_2}{r_2}\right) - \frac{1}{2}\omega^2(x^2+y^2) \tag{1.4}$$

Operating simple substitution, both equation of motion and potential function can be turned into a non-dimensional form. Defining new variables

$$\rho = \frac{r}{R}; \quad \xi = \frac{x}{R}; \quad \eta = \frac{y}{R}; \quad \zeta = \frac{z}{R}; \quad \tau = t \cdot \omega$$

and consequently

$$\frac{d}{dt} = \omega\frac{d}{d\tau}$$

Substituting and manipulating, non-dimensional equation of motion depending on potential function gradient will be derived:

$$\frac{\partial^2 \vec{r}}{\partial t^2} = -\boldsymbol{\nabla}\mathcal{U} - 2\boldsymbol{\omega} \wedge \frac{\partial \vec{r}}{\partial t} \tag{1.5}$$

The equation broken down into the three components along the non dimensional reference frame axis is:

$$\begin{cases} \dfrac{\partial^2 \xi}{\partial t^2} - 2\dfrac{\partial \eta}{\partial t} = \dfrac{\partial \mathcal{U}}{\partial \xi} \\ \dfrac{\partial^2 \eta}{\partial t^2} - 2\dfrac{\partial \xi}{\partial t} = \dfrac{\partial \mathcal{U}}{\partial \eta} \\ \dfrac{\partial^2 \zeta}{\partial t^2} = \dfrac{\partial \mathcal{U}}{\partial \zeta} \end{cases} \tag{1.6}$$

where

$$\mathcal{U} = \frac{1-\mu}{\rho_1} + \frac{\mu}{\rho_2} + \frac{1}{2}(\xi^2 + \nu^2)$$

is the gravitational potential equation, written in a dimensionless form. From the term above, some observations about the limits can be made: near m_1 or m_2 (thus with ρ_1 or ρ_2 near to zero) the potential will tends to infinity. On the other hand the function potential approaches the equation of a circle as ρ_1 or ρ_2 tend to infinity.

1.2.4 Derivation from potential equation

Keeping in mind the definition of Lagrangian points as locations in space where gravitational forces are balanced, thus velocities and accelerations w.r.t. rotating system are null, mathematical derivation could be made looking for these equilibrium points as minimum values of the potential function. This means solving the equation

$$\boldsymbol{\nabla}\mathcal{U} = 0$$

or in an explicit form, the system of equations:

$$\begin{cases} \dfrac{\partial \mathcal{U}}{\partial \xi} = 0 \\ \dfrac{\partial \mathcal{U}}{\partial \eta} = 0 \\ \dfrac{\partial \mathcal{U}}{\partial \zeta} = 0 \end{cases} \tag{1.7}$$

It is proved [5] that third equation, along the ζ axis, is verified when $\zeta = 0$, this means Lagrangian points are situated on the $\xi - \eta$ plane, as in figure 1.3.

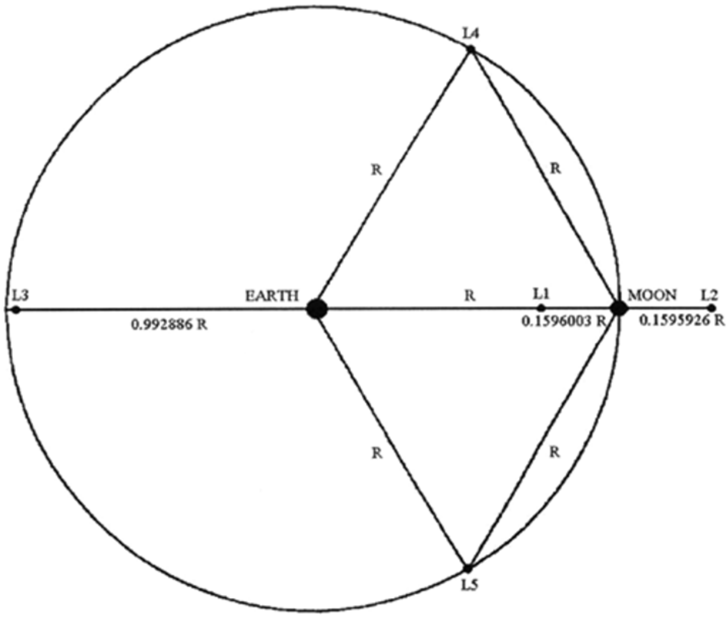

Figure 1.3: Graphical representation of the five Lagrangian point and their distance from Earth and Moon, expressed in terms of Earth-Moon distance R. Source: Ref [8]

In order to analytically find Lagrangian point positions in this plane, ξ axis will be analyzed separately. On ξ, axis joining the two bodies, Collinear Lagrangian Points (L1, L2 and L3) will be found. Graphically, solutions are sought as stationary points of the function obtained intersecting the potential $\mathcal{U}$ with the plane $\eta = 0$ or analytically solving equation:

$$\xi - \frac{1-\mu}{\rho_1^3}\left[\xi + \mu\right] - \frac{\mu}{\rho_2^3}\left[\xi - (1-\mu)\right] = 0 \tag{1.8}$$

Collinear Lagrangian points are finally defined as it follows:

- L1, also called *Cis-lunar* point, is found in the space between Earth and Moon. Imposing $\rho_1 + \rho_2 = 1$) it is obtained that L2 is located at about 15.8% of Earth-Moon distance.
- L2, also called *Trans-lunar*, is 61500 km beyond Moon and it's found imposing $\rho_1 - \rho_2 = 1$
- L3, also called Trans-Earth, is on the opposite side from the Moon, on the

same orbit.

There also are so called Equilateral points L4 and L5. They both are located in such a place that a equilateral triangles forms between Lagrangian points, Earth and Moon as in figure 1.3.

1.2.5 Jacobi's integral

Applying a scalar multiplication by $\frac{\partial r}{\partial t}$, to equation 1.5 and manipulating, the following equation is obtained

$$\frac{1}{2}\frac{dV^2}{d\tau} = \frac{d\mathcal{U}}{d\tau}$$

After integration, it becomes the so called *Jacobi's integral*

$$V^2 = 2\mathcal{U} - C \tag{1.9}$$

where V is the spacecraft velocity relative to the rotating frame; it is function of the potential $\mathcal{U}$ and Jacobi's constant of integration C, depends on initial position and velocity of the spacecraft.

This equation defines areas in space where motion is feasible: where the statement $V^2 > 0$ stands, thus where $C > 2\mathcal{U}$. Thanks to Jacobi's integral, a simple representation of fields of motion can be made: in fact they can be visualized by a line on $\mathcal{U} - V^2$ plane. Knowing both position and velocity, a bundle of lines will represents all possibility of motion by varying C, which basically depends on ΔV gained by the spacecraft at the beginning of the motion. In general a small value of C means the area of motion is bigger, so the spacecraft can reach further points in space.

Cases when $2\mathcal{U} - C = 0$ define the *surfaces of zero velocity* (or *Hill surfaces*), a boundary for regions accessible for the spacecraft in exam. Making an example, zero velocity surface passing by Lagrangian points are associated with a precise potential (obtained knowing the position) and C values in table 1.1. This means that one Lagrangian point can be reached only if C is smaller than the tabulated ones. Zero velocity surfaces can also be visualized, as closed lines which form by

Lagrangian point	$\mathcal{U}$	C
$L1$	1.5942	3.1885
$L2$	1.5361	3.1723
$L3$	1.5061	3.0122
$L4$	1.4940	2.9880
$L5$	1.4940	2.9880

Table 1.1: Potential $\mathcal{U}$ and Jacobi's constant C values for Lagrangian Points

intersection with horizontal planes xy as in figure 1.4.

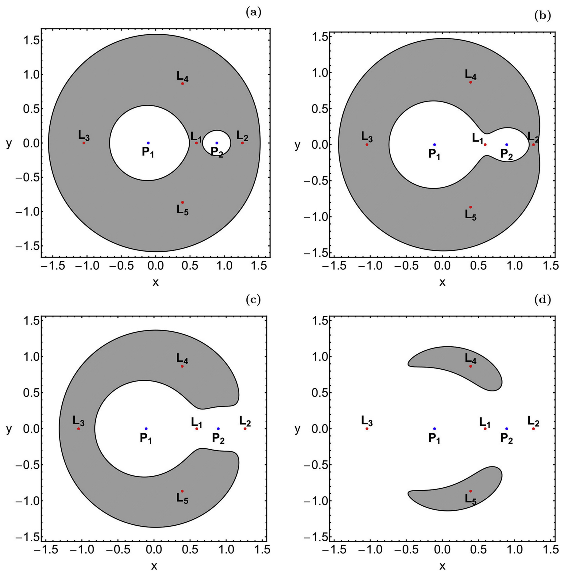

Figure 1.4: Intersection of the zero-velocity surfaces with xy plane for various values of C. Source: Ref [13]

Imagining to be in a precise point in space, with fixed $\mathcal{U}$, some qualitative considerations about fields of motions can be done, describing how they change when C is varying:

- When $C > C_{L1}$, two circles form around Earth and Moon. In this case a spacecraft can move only near the celestial bodies around which it's orbiting and can not reach the region around the other body (figure 1.4-a).

- When C decreases, circles turn into ovals and expand. When $C = C_{L1}$ they meet at L1 and this means that a spacecraft orbiting around Earth can reach at the Lagrangian point, but it will have a null velocity, without being able to reach the field of motion around the Moon.
- When $C < C_{L1}$ a spacecraft can move from the area around Earth to the area around Moon (figure 1.4-b).
- When $C < C_{L2}$ a spacecraft can escape from the system behind Moon (figure 1.4-c).
- When $C < C_{L3}$ a spacecraft can escape from the system behind Earth and inaccessible region shrinks only around L4 and L5 (figure 1.4-d).

1.3 Interplanetary trajectories

For first-order analysis, an interplanetary trajectory can be studied exploiting the patched-conics approximation. This means considering the motion of the spacecraft as in a two-body problem, thus gravitationally influenced by just one main celestial body. The spacecraft starts its journey under the influence of Earth, after escape it's under the influence of the Sun alone, until the arrival in proximity of the final destination, where only the target body gravity is taken into account.

From the above mentioned assumption follows the need to define certain boundaries where the main body, from the spacecraft point of view, should switch. Intuitively, on the boundary surface, accelerations caused by the two bodies perturbing the motion will be imposed as equivalent. To be rigorous, the final equivalence derives from the equation of motion for the n-body problem. The step-by-step derivation can be found in Cornelisse, Schöyer, and Wakker [5]. For the sake of conciseness, a brief description of the reasoning will follow.

Considering for instance the above-mentioned case of a probe sent towards deep space, it is possible to express its motion viewed from a fixed reference frame centered in Earth, thus considering acceleration caused by the Sun as the only perturbation:

$$A = A_e + A_{ps}$$

At the contrary, the probe can also be viewed from the Sun point of view, thus considering Earth responsible for the only perturbing acceleration.

$$a = a_s + a_{pe}$$

The equivalence between the two equations of motion, which in fact describe the same situation, results in:

$$\frac{a_{pe}}{a_s} = \frac{A_{ps}}{A_e}$$

Calculations from this equivalence will lead to the definition of a rotationally symmetric surface about the line joining celestial body centers of mass will be obtained. The surface encloses the so called Sphere of Influence (SOI) of the planet. Radius can be easily derived from the expression suggested by Laplace:

$$R_{s.i} = D\left(\frac{m}{M}\right)^{2/5}$$

where D is the distance between the two bodies considered; m is the smaller body mass and M is the larger body mass [1, pp. 333–334].

Chapter 2

Optimization method

2.1 Indirect method

An optimization problem by definition, aims to find the best solution among all the feasible solutions; this is often done exploiting a numerical method consisting in finding the right control law which maximizes or minimizes a specific performance index. As far as orbital transfers are concerned, minimizing fuel consumption is crucial in order to keep a low overall cost of the maneuver; that's why optimization purpose is to maximize the spacecraft final mass in the trajectories considered. As can be easily imagined, analytical solution of such a optimization problem is only possible for few simple cases, which are not interesting for the study, is therefore necessary to seek approximate solution through numerical methods.

The numerical method chosen is an indirect optimization technique. They are considered computationally very efficient, providing high accuracy with a good theoretical insight, moreover they have relatively low computational cost and time. On the other side, they result to be extremely sensitive to the guess values imposed as tentative solution. For this reason, choosing the right inputs was a delicate step in order to obtain the desired data and often required a long time both considering the number of guesses and the compile time. In the first place, guesses used in this analysis are from previous studies [9] analysing a similar problem. The hereafter explained method, is fully described in Arthur E Bryson and Yu-Chi Ho. *Applied optimal control: optimization, estimation, and control.* Routledge, 2018.

2.2 Optimal Control Theory (OCT)

2.2.1 Theoretical approach

Optimal Control Theory (OCT) is based on the concepts of variational calculus and it is applied to a generic differential equation system, having the form

$$\frac{d\boldsymbol{x}}{dt} = \boldsymbol{f}\left(\boldsymbol{x}, \boldsymbol{u}, t\right) \tag{2.1}$$

Equations above, also called *state equations*, describe state variables $\boldsymbol{x}$ evolution from initial time to final time (external boundaries) as function of control variables $\boldsymbol{u}$.

A convenient practice for orbital maneuvers optimization is breaking down the trajectory into several sub-ranges, called *arcs*, in which all variables are continuous. It is a useful practice in order to avoid numeric instabilities and improve convergence, providing high accuracy [11]. Notation adopted states that *j-ism* range begins at $t_{(j-1)_+}$ and ends at t_{j_-}, while variables at its boundaries are $\boldsymbol{x}_{(j-1)_+}$ and $\boldsymbol{x}_{j_-}$ (where subscripts *'+'* and *'-'* refers to the values respectively, right after and right before the point considered, so that any variable discontinuity can be accounted). In the case studied, thrusted arcs and coasting arcs will be separated, so there will be a velocity discontinuity at the ends of each range.

State equations shall be complemented by *boundary conditions*, expressed in the form

$$\boldsymbol{\chi}\left(\boldsymbol{x}_{(j-1)_+}, \boldsymbol{x}_{j_-}, t_{(j-1)_+}, t_{j_-}\right) = 0 \qquad j = 1, \ldots, n \tag{2.2}$$

where n is the number of arcs. Optimal boundary condition, derived from optimal condition imposition are expressed in equation 2.3.

$$\boldsymbol{\sigma}\left(\boldsymbol{x}_{(j-1)_+}, \boldsymbol{x}_{j_-}, \boldsymbol{\lambda}_{(j-1)_+}, \boldsymbol{\lambda}_{j_-}, t_{(j-1)_+}, t_{j_-}\right) = 0 \qquad j = 1, \ldots, n \tag{2.3}$$

They are usually non-linear expressions written for both state variables and independent time variable, at external boundaries and internal boundaries, among arcs.

That being said, optimum problem is solved, finding maximum and minimum values of the functional J, which is defined, in his generic form, as in equation 2.4.

$$J = \varphi\left(\boldsymbol{x}_{(j-1)_+}, \boldsymbol{x}_{j_-}, t_{(j-1)_+}, t_{j_-}\right) + \sum_j \int_{t_{(j-1)_+}}^{t_{j_-}} \Phi\left(\boldsymbol{x}(t), \boldsymbol{u}(t), t\right) dt \qquad j = 1, \ldots, n \tag{2.4}$$

The functional J is the sum of two parts: φ is function of the external values of state variables and time variable at the boundaries of each range; function ϕ is the integral over the whole trajectory and depends on variable values in every point. Introducing new suitable variables: constant Lagrange multipliers μ for boundary conditions and adjoint variables λ for state equations, the functional J can be written in a simplier form, like in equation 2.5.

$$J^* = \varphi + \boldsymbol{\mu^T}\boldsymbol{\chi} + \int_{t_{(j-1)_+}}^{t_{j_-}} \left(\Phi + \boldsymbol{\lambda}^T\left(f - \dot{\boldsymbol{x}}\right)\right) dt \qquad j = 1, \ldots, n \tag{2.5}$$

Through this new set of variables it is always possible to obtain a simplified form of the functional J^*: Lagrange formulation (where $\varphi = 0$) or Mayer formulation (where $\Phi = 0$). After making all these substitutions, the two functional J and J^* correspond, thus also their extremal values do, as long as boundary conditions and state equations are satisfied (thus $\boldsymbol{\chi} = 0$ and $\boldsymbol{f} - \dot{\boldsymbol{x}} = 0$).

In conclusion, the optimal condition is obtained when the statement $\delta J^* = 0$ is true for any value of $\delta\boldsymbol{x}_{(j-1)_+}, \delta\boldsymbol{x}_{j_-}, \delta t_{(j-1)_+}$ or δt_{j_-}; thus imposing appropriate values of μ and λ that make null $\delta\boldsymbol{x}$ and δt coefficients. Operating like said, two differential sets of equations are obtained: Eulero-Lagrange equations for adjoint variables

$$\frac{d\boldsymbol{\lambda}}{dt} = -\left(\frac{\partial H}{\partial \boldsymbol{x}}\right)^T \tag{2.6}$$

and algebric equations for controls

$$\left(\frac{\partial H}{\partial \boldsymbol{u}}\right)^T = 0 \tag{2.7}$$

where the function H is the Hamiltonian function, defined as

$$H = \Phi + \boldsymbol{\lambda}^T\boldsymbol{f} \tag{2.8}$$

The case with constraints on a control variable (for example when thrust modulus must be between 0 and T_{max}) has a particular relevance because Pontryagin's Maximum Principle (PMP) applies: the optimal control value in every point of the trajectory is the one which maximise the Hamiltonian (or minimize whether J maximum or minimum values are searched), so it is obtained solving equation 2.7. To be precise, two situation are possible: if optimal values of the control, is in the eligibility range, control is locally *'non-constrained'*; if solution from equation 2.7 is out of the eligibility range, the control assumes a value at the edge and it's called *'constrained'* control. It's worth noticing that if Hamiltonian is linear with respect to one or more controls, it won't appear in equation 2.7, subsequently the so called *bang-bang* control will be applied. Considering the control coefficient in equation 2.8: H is maximized with the maximum value of the control in case the corresponding coefficient is positive, with the minimum value in case the coefficient is negative.

2.2.2 Application to the case study

In the present study, state variable vector is defined by position and velocity in polar coordinate and the mass of the spacecraft

$$\boldsymbol{x} = \{r \quad \theta \quad \varphi \quad u \quad v \quad w \quad m\}^T$$

and adjoint variable vector will be

$$\boldsymbol{\lambda} = \{\lambda_r \quad \lambda_\theta \quad \lambda_\varphi \quad \lambda_u \quad \lambda_v \quad \lambda_w \quad \lambda_m\}^T$$

while the only control variable is thrust vector $\boldsymbol{T}$ (its direction and magnitude). Considering Mayer formulation, Hamiltonian becomes

$$H = \boldsymbol{\lambda}^T \boldsymbol{x} = H' + \boldsymbol{\Lambda T} - \lambda_m \left(\frac{T}{c}\right)$$

where H' is a term containing all parts without the control and

$$\Lambda = \lambda_u \boldsymbol{i} + \lambda_v \boldsymbol{j} + \lambda_v \boldsymbol{k}$$

the *primer vector*, is the adjoint vector to velocity.

It's easy to note that Hamiltonian function is linear with respect to the control variable T, thus the PMP is used, applying the before mentioned *bang-bang* control. Stated that optimal thrust direction is parallel to $\boldsymbol{\lambda}$, Hamiltonian can be rewritten as

$$H = H' + T\left(\frac{\Lambda}{m} - \frac{\lambda_m}{c}\right) \tag{2.9}$$

where thrust coefficient is called Switching Function (SF) and Λ indicate the primer vector magnitude. Optimal control values will subsequently be

$$T = \begin{cases} T_{max} & \text{for } SF > 0 \\ 0 & \text{for } SF < 0 \end{cases}$$

Since control value is discontinuous, division in arcs is applied when the SF sign changes. The number and nature of trajectory arcs is assumed a priori, but correspondence is checked and eventually modified, at the end of the numerical procedure.

2.3 Boundary Values Problem (BVP)

From Optimal Control Theory (OCT) application, it is understood that some initial values of the variables are unknown, so optimization will come from the solution of the Boundary Values Problem (BVP), which comprehends differential equations 2.1 and 2.6, with controls determined by equations 2.7 and boundary conditions from equations 2.2 and 2.3. The main difficulty in indirect methods arises in the solution of the BVP: the above mentioned equations are adapted to the type of problem and they are integrated by using a variable-order variable-step scheme, based on the Adams-Moulton formulas. BVP is divided into several Initial Value Problem (IVP) and it is solved using a Newton-like method, until convergence, which occurs when initial values satisfy all boundary conditions. In this section, implementation of indirect method for our analysis with the BVP formulation as well as solving procedure will be explained.

2.3.1 Formulation of the problem

State variables and adjoint variables are mashed together in one vector $\boldsymbol{y} = (\boldsymbol{x}, \boldsymbol{\lambda})$, creating one big 14 equation system:

$$\frac{d\boldsymbol{y}}{dt} = \boldsymbol{f}^* (y, t) \tag{2.10}$$

Initial values of the state variables is assigned, as well as the final radius (both in the case of escape or interplanetary trajectory); instead the 7 adjoint variables and the length of the burn and coast arc are unknown at the initial time. A replacement for independent time variable is replaced by variable ϵ, so that internal and external boundaries are fixed equals to progressive integer numbers like in equation

$$\varepsilon = j - 1 + \frac{t - t_{j-1}}{\tau_j} \tag{2.11}$$

where $\tau_j = t_j - t_{j-1}$ is the duration of the single range, which remain unknown. Now applying the change of variable and separating variable and constant parameter in $\boldsymbol{y}$, what it is obtained is

$$\frac{d\boldsymbol{z}}{d\varepsilon} = \boldsymbol{f} (\boldsymbol{z}, \varepsilon) \tag{2.12}$$

where $\boldsymbol{z} = (\boldsymbol{y}, \boldsymbol{c})$. Also boundary conditions (imposed and for optimality) are gathered in a single vector:

$$\boldsymbol{\Psi}(\boldsymbol{s}) = 0 \tag{2.13}$$

where vector $\boldsymbol{s} = (\boldsymbol{y}_0, \boldsymbol{y}_1, \ldots, \boldsymbol{y}_n, \boldsymbol{c})$ contains the values of all the variables at the edges of every range. Finally $\boldsymbol{p}$ is defined as the vector of the unknowns, containing all the initial values .

2.3.2 Numerical solution

Unknowns are find with an iterative process, starting from a guess solution $\boldsymbol{p}^1$ and integrating differential equations along the trajectory. At the end, the values of the state variables at the boundaries are determined and placed in the vector $\boldsymbol{\Psi}^r$ (where the apex r indicates the current iteration). Error on the boundaries condition $\Delta\boldsymbol{\Psi}$ can be evaluated, considering that a variation in initial conditions brings to a variation on boundaries, equals to

$$\Delta\boldsymbol{\Psi} = \left[\frac{\partial\boldsymbol{\Psi}}{\partial\boldsymbol{p}}\right]\Delta\boldsymbol{p} \tag{2.14}$$

Since the aim is to nullify the error (having $\Delta\boldsymbol{\Psi} = -\boldsymbol{\Psi}^r$), initial values must be corrected in amount equals to

$$\Delta\boldsymbol{p} = \boldsymbol{p}^{r+1} - \boldsymbol{p}^r = -\left[\frac{\partial\boldsymbol{\Psi}}{\partial\boldsymbol{p}}\right]^{-1}\boldsymbol{\Psi}^r \tag{2.15}$$

where the matrix $\left[\frac{\partial\boldsymbol{\Psi}}{\partial\boldsymbol{p}}\right]$ can be obtained either solving the homogeneous problem or numerically, firstly perturbing each Ψ component by a small amount and then integrating equation 2.12.

At this point the initial condition vector for the following iteration can be obtained:

$$\boldsymbol{p}^{r+1} = \boldsymbol{p}^r + K_R\Delta\boldsymbol{p} \tag{2.16}$$

where $K_R = 0.1 \div 1$ is called relaxation fraction and it's used for reducing the correction and avoid to compromise convergence. The scheme is repeated until error is lower than a certain threshold.

2.4 Structure of the code implementing the method

2.4.1 User interface

Optimization method explained in the previous section has been implemented in a code written in FORTRAN language, a language designed for computationally intensive applications in science and engineering. As above mentioned in our problem the *switching structure* is decided a priori, for this reason different codes were created according to different mission concepts. In particular three codes were adopted in the present study:

- `el2moon2ofc3` implementing a single-burn escape maneuver, divided into 2 phases;

- `el2moon4ofc3` implementing a double-burn escape maneuver, with 4 phases;
- `esarv1` is the code used for the interplanetary maneuver, which is considered as a single phase maneuver, even if the number of burns is more than one, according to the Switching Function (SF) sign.

The codes were used exclusively through user interface implemented on-screen by an (`.exe`) extension application which can be opened with any Microsoft Windows operating system. After initialization requests (integration step required and maximum number of iteration), user shall manually enter all constraints values: initial time t_0, mission duration `Dt`, final energy c_3 and final time for internal boundaries between arcs (this is the only value always set as free). The possibility to not constrain certain values remains available, simply by setting the value equal to 0. With the strategy adopted, initial time was always constrained, while one parameter between duration and final energy was left free.

2.4.2 Structure and subroutines

All the codes have a similar structure; with the aim to explain its functioning, we divide the script into sections having different purposes. The main ones are briefly explained below.

Initialization

First lines are meant to introduce the variables of the problem, initial conditions, useful parameters and conversion constants used throughout the code to linearize variables with respect to the current reference frame. In this part celestial bodies positions are found with external function `eph3d` which uses *JPL ephemeris* to calculate Moon and Sun positions with respect to Earth. Also perturbing accelerations are calculated with the help of other function (such as `geopot`).

function `BVNGL`

This function has the task to calculate tentative solutions, necessary during integration phase; verify whether Pontryagin principle is accomplished and in case of convergence, it saves the variables in the solution vector.

subroutine `FUNZ`

In this part differential equation of the problem are implemented, setting up the entire problem. It uses as inputs current phase index, independent variable time and instantaneous state variable vector; providing derivative vector as output.

subroutine `BOUND`

This subroutine calculates error on boundary conditions, providing as output vector `ER`. External boundary condition vector, and current state variable vector are the inputs.

Chapter 3

Dynamic model

3.1 Reference frames

3.1.1 Earth Mean Equator and Equinox of Epoch J2000 (EME2000)

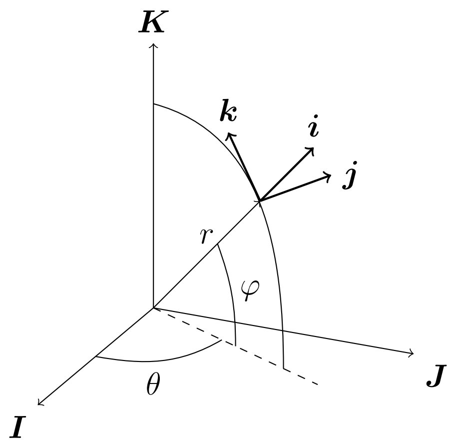

Figure 3.1: EME2000 and topocentric reference frame

The reference frame adopted in this study is the Earth Mean Equator and Equinox of Epoch J2000 (EME2000) (in figure 3.1) having its origin on Earth center of mass; equator as fundamental plane and x-axis lying along the line created by the intersection between Earth equator and the ecliptic. Its axes are denoted by unit vectors $\boldsymbol{I}$,$\boldsymbol{J}$,$\boldsymbol{K}$, positions are described with polar coordinates radius r, right ascension θ and declination φ:

$$\boldsymbol{r} = r\cos\theta\cos\varphi\boldsymbol{I} + r\sin\theta\cos\varphi J + r\sin\varphi\boldsymbol{K}$$

Velocities are defined in a topocentric reference frame, with components u along the radial (or zenith) direction i, v pointing eastward along the j axis and w pointing northward along k axis.

This local reference frame can be found by performing two simple rotations:

- the first around $\boldsymbol{K}$ by an amount equals to right ascension θ, will find a back-up reference frame ($\boldsymbol{tjK}$) where $\boldsymbol{K}$ remains the same;

$$\boldsymbol{r}_{tjK} = \begin{bmatrix} \cos\theta & \sin\theta & 0 \\ -\sin\theta & \cos\theta & 0 \\ 0 & 0 & 1 \end{bmatrix} \boldsymbol{r}_{IJK} \tag{3.1}$$

- a second rotation about $\boldsymbol{j}$ axis by an amount equals to declination (actually a negative rotation, clockwise) will lead to the topocentric frame $\boldsymbol{ijk}$

$$\boldsymbol{r}_{ijk} = \begin{bmatrix} \cos-\varphi & 0 & -\sin-\varphi \\ 0 & 1 & 0 \\ \sin-\varphi & 0 & \cos-\varphi \end{bmatrix} \boldsymbol{r}_{tjK} \tag{3.2}$$

Mathematically, these rotations are expressed by a chained matrix product, where multiplying simple rotation matrices written above, the final transformation matrix is found.

$$\begin{aligned} \boldsymbol{r}_{ijk} &= L_\varphi^j \cdot L_\theta^K \quad r_{IJK} \\ &= L \quad r_{IJK} \end{aligned} \tag{3.3}$$

or explicating vectors and matrix:

$$\begin{Bmatrix} \boldsymbol{i} \\ \boldsymbol{j} \\ \boldsymbol{k} \end{Bmatrix} = \begin{bmatrix} \cos\theta\cos\varphi & \sin\theta\cos\varphi & \sin\varphi \\ -\sin\theta & \cos\theta & 0 \\ -\cos\theta\sin\varphi & -\sin\theta\sin\varphi & \cos\varphi \end{bmatrix} \begin{Bmatrix} \boldsymbol{I} \\ \boldsymbol{J} \\ \boldsymbol{K} \end{Bmatrix} \tag{3.4}$$

It should be noted that geocentric reference frame has been used as far as escape trajectories are concerned; instead for interplanetary trajectories analysis an heliocentric reference frame has been deemed appropriate. Variables were subsequently normalized with respect to Earth radius (for geocentric reference frame) and Sun-Earth distance (for heliocentric).

3.1.2 Equations of motion

The statement of the problem is the same described in previous analysis, as in article by Lorenzo Casalino, Guido Colasurdo, and Dario Pastrone. "Optimal low-thrust escape trajectories using gravity assist". In: *Journal of Guidance, Control, and Dynamics* 22.5 (1999), pp. 637–642. In the present study the spacecraft is considered as a point-mass with variable mass and its motion is described by the following equations:

$$\frac{d\boldsymbol{r}}{dt} = \boldsymbol{V} \tag{3.5}$$

$$\frac{d\boldsymbol{V}}{dt} = -\frac{\mu\boldsymbol{r}}{r^3} + \frac{\boldsymbol{T}}{m} + \boldsymbol{a}_p \tag{3.6}$$

$$\frac{dm}{dt} = -\frac{T}{c} \tag{3.7}$$

where the effective exhaust velocity c is assumed constant and the perturbing acceleration

$$\boldsymbol{a}_p = \boldsymbol{a}_J + \boldsymbol{a}_{lsg} + \boldsymbol{a}_{srp}$$

comprehends accelerations caused by Earth asphericity, Sun and Moon gravity (lunisolar perturbation) and Solar Radiation Pressure (SRP). Position $\boldsymbol{r}$, velocity $\boldsymbol{V}$ and mass m described in the differential equations above, are the state variable of the problem; thrust vector $\boldsymbol{T}$ controls the trajectory.

3.2 State equations

Given the above mentioned reference frame, scalar state equations are easily derived:

$$\frac{dr}{dt} = u \tag{3.8}$$

$$\frac{d\theta}{dt} = \frac{v}{r\cos\varphi} \tag{3.9}$$

$$\frac{d\varphi}{dt} = \frac{w}{r} \tag{3.10}$$

$$\begin{aligned} \frac{du}{dt} = & -\frac{1}{r^2} + \frac{v^2}{r} + \frac{w^2}{r} + \frac{T}{m}\sin\gamma_T + \frac{qS}{m}\big[-C_D\sin\gamma + \\ & + C_L\cos\sigma\cos\gamma\big] \end{aligned} \tag{3.11}$$

$$\begin{aligned} \frac{dv}{dt} = & -\frac{uv}{r} + \frac{vw}{r}\tan\varphi + \frac{T}{m}\cos\gamma_T\cos\psi_T + \frac{qS}{m}\big[-C_D\cos\gamma\sin\psi + \\ & + C_L\big(-\cos\sigma\sin\gamma\cos\psi + \sin\sigma\sin\psi\big)\big] \end{aligned} \tag{3.12}$$

$$\begin{aligned} \frac{dw}{dt} = & -\frac{uw}{r} + \frac{v^2}{r}\tan\varphi + \frac{T}{m}\cos\gamma_T\sin\psi_T + \frac{qS}{m}\big[-C_D\cos\gamma\sin\psi + \\ & + C_L\big(-\cos\sigma\sin\gamma\cos\psi + \sin\sigma\sin\psi\big)\big] \end{aligned} \tag{3.13}$$

$$\frac{dm}{dt} = -\frac{T}{c} \tag{3.14}$$

In equations above, perturbing acceleration are made explicit, bringing to light new angles which have to be defined: γ is *flight path angle*, identified between relative velocity vector $\boldsymbol{V}_r$ and the horizontal plane (with positive angles upwards, moving away from origin); ϕ is *heading* angle measured between relative velocity $\boldsymbol{V}_r$ projection on horizontal plane and j axis (with positive angles counterclockwise); γ_T and ϕ_T are the same angles, for Thrust vector $\boldsymbol{T}$; σ is called *roll angle* or *bank angle*, i.e. the angle between aerodynamic lift L and the trajectory plane (identified by vectors $\boldsymbol{r}$ and $\boldsymbol{V}$) measured clockwise from radial direction.

It's worth noting that γ and ϕ depend on state variables as in the following relations:

$$\sin\gamma = \frac{u}{V_r} \tag{3.15}$$

$$\cos\gamma\cos\phi = \frac{v - \omega r\cos\varphi}{V_r} \tag{3.16}$$

$$\cos\gamma\sin\phi = \frac{w}{V_r} \tag{3.17}$$

where $V_r = \sqrt{u^2 + (v - \omega r\cos\varphi)^2 + w^2}$ is relative velocity modulus, which takes account of Earth rotation velocity directed eastward.

Angles γ_T and ϕ_T define thrust direction, their optimal values are derived by imposing equals to zero Hamiltonian partial derivatives:

$$\sin\gamma = \frac{\lambda_u}{\lambda_V} \tag{3.18}$$

$$\cos\gamma\cos\phi = \frac{\lambda_v}{\lambda_V} \tag{3.19}$$

$$\cos\gamma\sin\phi = \frac{\lambda_w}{\lambda_V} \tag{3.20}$$

where it's worth remembering that primer vector modulus λ_V result parallel to thrust optimal direction.

3.3 Perturbations

As mentioned before, a spacecraft motion in space, particularly in the 4-body problem here considered, is extremely complicated to describe because of the numerous forces in action. The spacecraft position along the trajectory could be affected by disturbing forces, causing a deviation from original path. That's why perturbations should be taken into account and a position control law it is always necessary. Specifically, in the case studied, the only disturbance considered are J2 effect due to Earth oblateness, Lunisolar perturbation and Solar Radiation Pressure (SRP). Atmospheric drag is neglected because of the great distance of the spacecraft from Earth atmosphere during the whole trajectory, as well as for Moon potential model which can be implemented in future studies; other perturbations that affect the attitude aren't obviously taken into account, considering a point-mass instead of a dimensional spacecraft for this part of the study.

3.3.1 Earth Potential Model

Even though spacecraft trajectories investigated in this study are far away from Earth, so its potential actually don't affect the spacecraft position that much, it was modeled anyway, for the sake of completeness and to ease future studies which may include trajectories closer to Earth. The model considered is based on Earth Gravitational Model 2008 (EGM2008) provided by the National Geospatial-Intelligence Agency (NGA), which have a 2.5 minute height resolution (resulting in 4.2 km at equator)[6] and depicted in figure 3.2. According to EGM2008, the

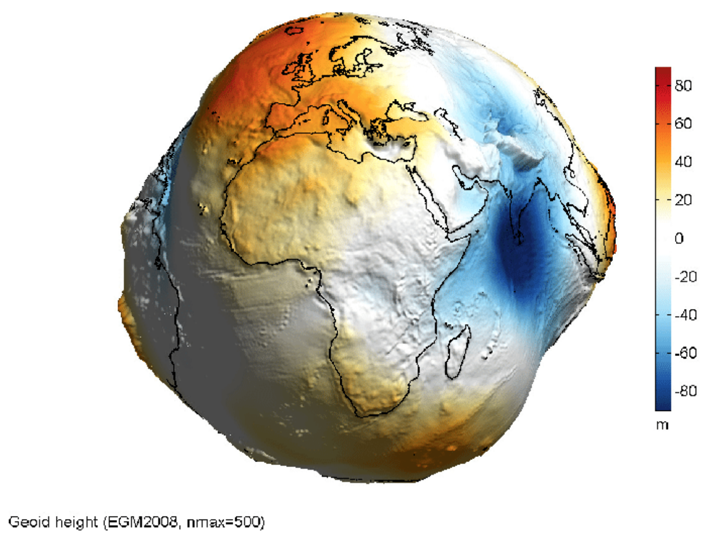

Figure 3.2: Geoid height, computed from the gravity field model EGM2008(Pavlis et al., 2012). Source: Ref [2]

potential is calculated using the expression, where the number of harmonics N was chosen equal to 8:

$$\Phi_{EG} = -\mu_{\oplus} r \sum_{n=2}^{N} \left(\frac{r_E}{r}\right)^n \sum_{m=0}^{n} \left(C_{nm} \cos m\lambda + S_{nm} \sin m\lambda\right) P_{nm} \left(\sin \varphi\right) \tag{3.21}$$

where μ is Earth gravitational parameter; r_E is the ellipsoid semimajor axis; φ and λ are respectively latitude (equal to declination) and longitude (derived considering Earth angular velocity) ; $P_{nm}(\sin\varphi)$ are the Legendre functions; C_{nm} and S_{nm} are the coefficients for spherical and sectorial or tesseral harmonics [11].

3.3.2 Lunisolar Perturbation

Even though Earth is considered as main celestial body in the reference frame adopted, also Moon and Sun gravity affect the motion of the spacecraft. Forces imposed on the spacecraft strictly depend on its relative position with respect to other celestial: positions with respect to Earth are provided by DE430JPL ephemerides database and expressed in the International Celestial Reference Frame (ICRF) which can be considered the same as EME2000 thanks to minimal differences between them. The position of the body can be expressed as

$$r_b = x_b\boldsymbol{I} + y_b\boldsymbol{J} + z_b\boldsymbol{K}$$

where the subscript b varies whether Sun or Moon are considered. Generic acceleration to which the spacecraft is subjected, is expressed by

$$\boldsymbol{a}_{bg} = -\left(\frac{\mu_b}{R^3}\right)\boldsymbol{R} - \left(\frac{\mu_b}{r_b^3}\right)\boldsymbol{r}_b \tag{3.22}$$

where $\boldsymbol{R} = r - r_b$ is the spacecraft relative position. The projection in the topocentric reference frame, used in this study, it becomes:

$$(a_{bg})_u = \left(\frac{\mu_b}{R^3}\right)[(r_b)_u - r] - \left(\frac{\mu_b}{r_b^3}\right)(r_b)_u \tag{3.23}$$

$$(a_{bg})_v = \left(\frac{\mu_b}{R^3}\right)(r_b)_v - \left(\frac{\mu_b}{r_b^3}\right)(r_b)_v \tag{3.24}$$

$$(a_{bg})_w = \left(\frac{\mu_b}{R^3}\right)(r_b)_w - \left(\frac{\mu_b}{r_b^3}\right)(r_b)_w \tag{3.25}$$

They are function of the body positions, thus function of variables r, θ and φ. Obviously, the total lunisolar perturbation is the sum of Moon perturbation and

Sun perturbation:

$$(a_{lsp})_u = (a_l g)_u + (a_s g)_u \tag{3.26}$$

$$(a_{lsp})_v = (a_l g)_v + (a_s g)_v \tag{3.27}$$

$$(a_{lsp})_w = (a_l g)_w + (a_s g)_w \tag{3.28}$$

3.3.3 Solar Radiation Pressure (SRP)

Solar Radiation Pressure (SRP) is a disturbing force coming from the pressure variation due to photons impacting the spacecraft surface which is about $4.55682 \cdot 10^{-6}\, N/m^2$ near Earth. It is a small value but can affect the spacecraft attitude and position in the long period, even though its effect is not so important in the trajectories studied, implementation of the disturbance is taken into account for sake of completeness. Perturbing acceleration due to SRP is expressed in the following equation:

$$a_{srp} = (1+\eta)\left[\frac{L_s}{4\pi c R^3}\right]\left(\frac{S}{m}\right)\boldsymbol{R} \tag{3.29}$$

where η is the reflectivity factor (assumed $\eta = 0.7$) which depends by the material and orientation of the surface; $L_s = 3.83 \cdot 10^2 6\, W$ is the total power radiated by the Sun; S is the spacecraft perpendicular surface impacted by solar radiation; the vector $\boldsymbol{R}$ indicate that this force act on the line joining the Sun and the spacecraft, moving away from the Sun.

Chapter 4

Procedure and results

In this chapter procedure adopted for this research will be explained and results will be analyzed. The main steps of the work done include the definition of the mission features considered suitable for the study; data collection for the phase concerning escape from Earth SOI and finally data collection for the whole trajectory towards NEA, thus the addition of the interplanetary part.

4.1 Definition of the case study mission

The mission profile considered, is a medium-size satellite placed in correspondence of EML2, performing an escape maneuver till the boundary of the Earth SOI, then connected with an interplanetary trajectory heading towards a specific asteroid named 2016 TB57, belonging to NEA. Technical specifications are set according to the previous studies concerning the same topic [9] and they can be found in the first part of the code, as mentioned in section 2.4. Initial mass is $m_i = 850kg$ (identified by the variable `amrif`), specific impulse is $I_{sp} = 2000s$ (variable `aisp`), as a typical Hall effect thruster.

Five dates were selected for the analysis as departure time for the mission, with a time span covering the *synodic period* of the Moon orbit (defined as the time it takes for the Moon to rotate around Earth until the same relative position among Moon, Earth and Sun is restored). Time is actually measured in as non-dimensional, with such a conversion that zero instant is set, as epoch J2000, on

1^{st} January 2000 and the following days are obtained with a proportion, considering that 1year $= 2\pi$. In table 4.1 departure times considered are listed and the corresponding day/month/year form is obtained. It is noteworthy that departure

Case	Departure Time	Departure Date
1	162.033	15/10/2025
2	162.153	22/10/2025
3	162.274	29/10/2025
4	162.394	05/11/2025
5	162.514	12/11/2025

Table 4.1: Time conversion at initial point of the maneuver

times are one week apart from each other so that an entire month it's covered, this is important because relative angle between the spacecraft and the Sun affect the orbital motion, resulting either in a positive or negative perturbation.

4.2 Escape from Earth-Moon Lagrangian Point 2 (EML2)

The first part of the trajectory is the evasion from Earth SOI: initial point is obviously EML2 position, instead final point of escape maneuver is set 3 million km away from Earth, applying a constraint to the radial distance from the EME2000 reference frame origin.

The strategy consists in assuming two phases during escape: the first one is a thrusted arc, tagged with letter "T"; second one is a coasting arc tagged with letter "C". Solution is initially sought in this configuration, nevertheless, if optimization process leads to a positive result, output file that contains Switching Function (SF) values in every point will be checked. As mentioned in chapter 2, the SF is a crucial element for the thrust control: a positive value means that the thruster is on, instead with negative SF the thruster is off. That being said, in a T-C trajectory, SF should change sign (from positive to negative) only once, on the contrary a 4-phase approach with two burns should be investigated and optimization results should be adjourned using the output given from the appropriate code.

Six different scenarios are taken into account for the analysis: the first three with constrained duration for the escape maneuver (*75 days*, *80 days* and *90 days*) and free final energy; the latter three with fixed C3 ($0.2\,km^2/s^2$, $0.3\,km^2/s^2$ and $0.5\,km^2/s^2$) and free time to escape. The code solves Boundary Values Problem (BVP) and finally finds the optimal trajectory, respecting the constraints.

4.2.1 Escape with constrained duration

The procedure which leads to produce the needed data, starts from solutions coming from previous studies [9] having the same departure times. Specifically, solutions closest to the sought cases are chosen as starting point, then the method consists in changing the duration constraint, by a varying small amount of time in order to reach, step by step, the solutions sought in the present study. The number of steps it took to arrive to the desired final time, varied from case to case, in general it was more difficult to reach the longer duration cases (90 days), in particular for cases 2, 4 and 5 (see table 4.1); here one step could be as small as $0.1\,day$, implying a few dozen optimizations until reaching the one with the established constraints.

Solutions obtained in term of duration of the propelled arc and fuel mass consumed, are listed in table 4.2 and depicted in the histogram graph in figure 4.1.

Must be highlighted that case 2 solutions (rows in bold type in table 4.2) are calculated considering a 4-phase approach with two burns (T-C-T-C), for the reason explained in this section. In this case the T arc duration is intended as the sum of phase 1 and phase 3. For sake of preciseness the duration of the two separated T-arc are made explicit:

- In the 75-day scenario, optimal trajectory beginning at $t_0 = 162.153$ consists in a first burn with duration of 1.87 days and a second one, approximately one week later, with duration 0.37 days
- In the 80-day scenario, first and predominant thrust lasts 1.84 days then a second tiny burn is given right after, but the duration results irrelevant, thus

Departure Time	Duration $[days]$	T arc duration $[days]$	Final c_3 $[kg^2/s^2]$	Fuel consumption $[kg]$
162.033	75	1.79	0.35	2.111
162.153	**75**	**2.25**	**0.15**	**2.647**
162.274	75	5.90	$-6.41 \cdot 10^{-4}$	6.961
162.394	75	1.42	0.18	1.670
162.514	75	1.89	0.44	2.224
162.033	80	1.88	0.40	2.219
162.153	**80**	**1.84**	**0.10**	**2.172**
162.274	80	5.57	0.02	6.572
162.394	80	1.36	0.12	1.599
162.514	80	1.95	0.45	2.299
162.033	90	2.18	0.43	2.571
162.153	**90**	**1.53**	**0.07**	**1.810**
162.274	90	5.07	0.04	5.979
162.394	90	1.30	0.09	1.529
162.514	90	2.09	0.45	2.463

Table 4.2: Fuel Consumption for escape missions with constrained Dt and free c3

it's approximately a single burn trajectory

- Also in the 90-day scenario beginning at the same time, almost the total amount of thrust is given in the first burn.

Looking at the results obtained, it's worth noting that even with the same duration constraint, optimization leads to different solutions depending on the departure date and the variation in fuel consumption draws a wave pattern if imagined in a graph in a simple function of time. This is due to the relative position of the spacecraft with respect to other celestial bodies and due to the Sun perturbation which depends on the angular position between the spacecraft and the Sun in the first part of the trajectory. Solar perturbation could accelerate or slow down, acting whether in a positive or negative way depending on the situation and the mission target. With the purpose to investigate this phenomenon, angles between Moon and Sun at the initial point will be tabulated (table 4.3). Keeping

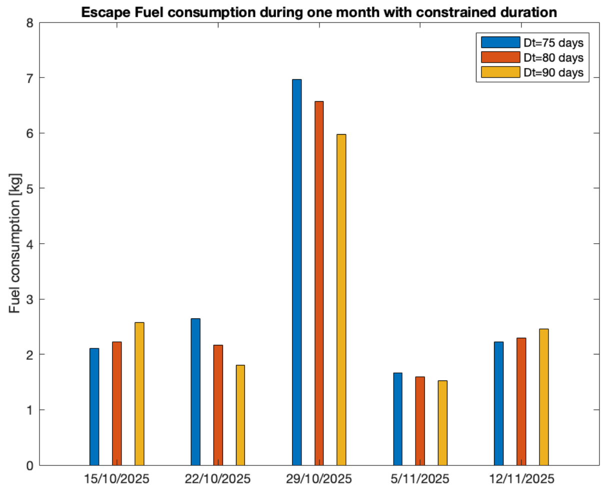

Figure 4.1: graphical display of the amount of fuel consumed to escape having a constraint in duration Dt

in mind that Earth, Moon and spacecraft in EML2 are aligned, thus angle $\theta_☾$ Sun and Moon position vectors corresponds to the angle of our interest. For helping the visualization, relative positions of Moon, Earth and Sun are depicted in figure 4.2 (online 3D simulator was used for this purpose [12]).

Case	Departure Time	Moon angle [deg]
1	162.033	115.27
2	162.153	201.73
3	162.274	310.58
4	162.394	34.47
5	162.514	116.43

Table 4.3: Moon angle $\theta_☾$ at departure time in EML2

Considering both histogram in figure 4.1 and data in table 4.2, best time for departure to escape seems to be 5/11/2025 (case 4) when the obtained fuel consumption results to be minimized. Probably in this case velocity direction at burn out is in the same direction of the Sun perturbation.

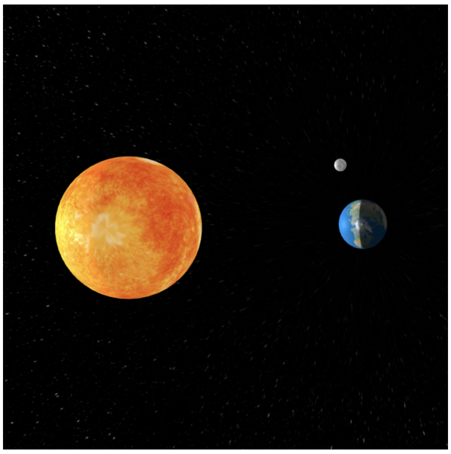

(a) *15/10/2025*

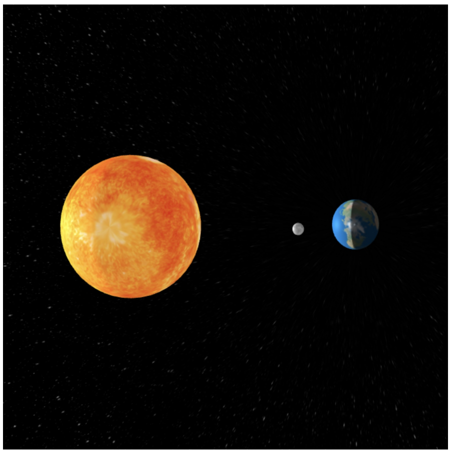

(b) *22/10/2025*

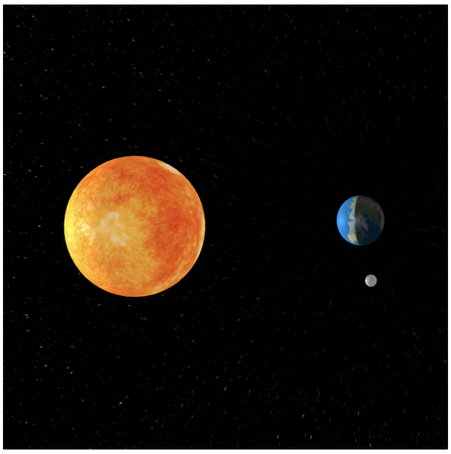

(c) *29/10/2025*

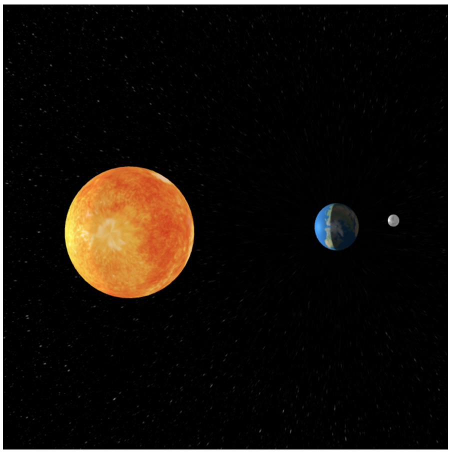

(d) *5/11/2025*

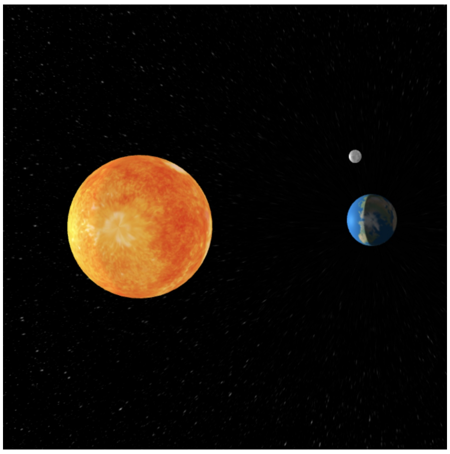

(e) *12/11/2025*

Figure 4.2: Representation of Sun, Earth and Moon relative positions (not in scale)

Other considerations can be made, looking at the variation of fuel required in relation with duration. When solar perturbation has a negative effect on the spacecraft (cases 2 and 3) fuel consumption decreases with the increasing of mission duration. That's because a longer time allows the spacecraft to reach a favorable position during coasting arc. On the contrary, when departure date is favorable, a longer time will force the spacecraft towards non convenient positions. Optimum in this sense is guaranteed in case 4, as said before.

4.2.2 Escape with constrained final energy

Procedure to obtain solutions when final energy set as constraint, is basically the same. In this case difficulties arose when seeking cases with low final energy ($c_3 = 0.2\, km^2/s^2$ and $c_3 = 0.3\, km^2/s^2$), especially in case 3 (table 4.1), requiring a $0.1\, km^2/s^2$ step. Again, solutions obtained in term of duration of the propelled arc and fuel mass consumed, are listed in table 4.4. Also in this case, rows in bold type are obtained with a four-phase approach (T-C-T-C trajectory). In particular:

- Case 2 has a 2.36 day long first burn, while the second thrust is almost 5 days later and lasts for about 1 hour 40 minutes;
- Case 3 has a 1.03 day long first burn and a 1.68 day long second burn 8 days later.

From the histogram in figure 4.3 some observations can be made: once again, the mean value of fuel required for escape seems varying depending on departure date and for the majority of the cases considered, a greater amount of fuel is necessary increasing the value of final energy c_3 imposed as constraint. This happens because a greater energy at the end of the maneuver means having a greater velocity, which is granted by a greater thrust. It's clear that case 3, with departure on 29/10/2025, is different: firstly it's the one minimizing the overall cost, moreover allows at the same time a great final energy with a low consumption, always useful characteristic if the aim is to reach far objects in deep space. This justifies the conclusion that there are different optimal trajectories on the basis of the mission target chosen; departure time isn't the only aspect to consider, but just

Departure Time	Final c_3 $[kg^2/s^2]$	T-arc $[days]$	Fuel consumption $[kg]$	Total duration $[days]$
162.033	0.2	1.70	2.004	78.59
162.153	**0.2**	**2.43**	**2.866**	**75.50**
162.274	**0.2**	**2.71**	**0.752**	**80.81**
162.394	0.2	1.44	1.693	73.93
162.514	0.2	1.83	2.161	78.42
162.033	0.3	1.72	2.032	75.89
162.153	0.3	3.15	3.716	71.45
162.274	0.3	2.40	2.824	86.84
162.394	0.3	1.59	1.873	69.00
162.514	0.3	1.84	2.169	74.76
162.033	0.5	3.18	3.745	74.45
162.153	0.5	5.41	6.374	61.40
162.274	0.5	0.73	0.863	72.74
162.394	0.5	2.84	3.351	62.79
162.514	0.5	2.46	2.902	77.22

Table 4.4: Fuel Consumption for missions with constrained final energy $c_3 = 0.3$

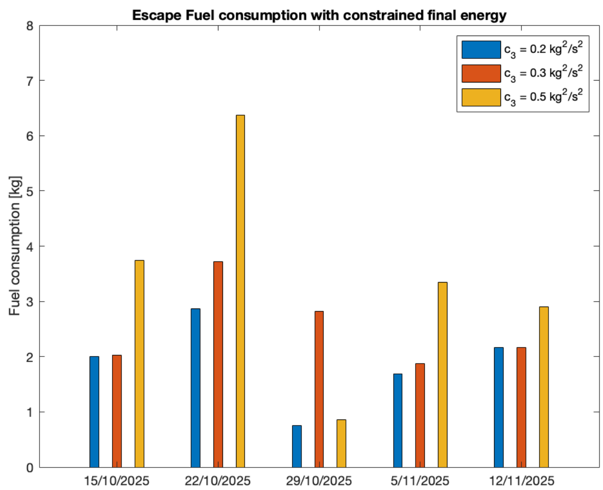

Figure 4.3: Graphical display of the amount of fuel consumed to escape having a constraint in c3

one variable which influences the behavior of a small spacecraft motion in the complex Earth-Moon-Sun system.

4.2.3 Optimal escape trajectory analysis

With an overall view of the data obtained (visualized in figure 4.4), it is clear that every departure date has local optimum, obtained with a precise combination of duration Dt and final energy c_3. These optimal trajectories were manually detected by seeking the highest final mass, thus the lowest fuel consumption. Cases

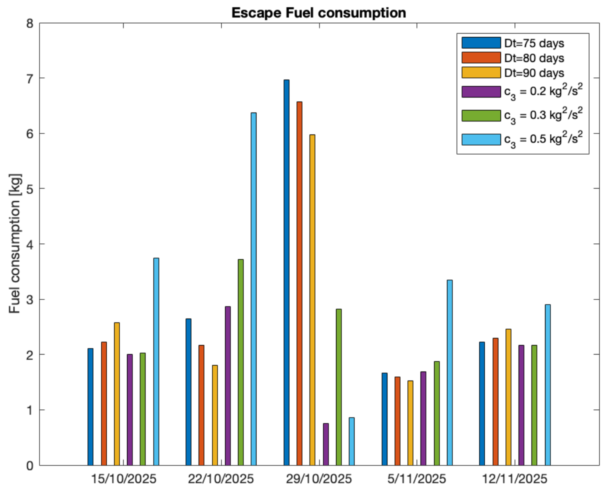

Figure 4.4: Graphical display of the amount of fuel consumed to escape

considered, listed in table 4.5, are worthy of further analysis coming from a spatial representation. Two cases were actually considered in cases 2,3 and 4, because data with similar escape duration, showed discordant results in final energy.

Trajectory plots on xy plane in Geocentric Equatorial reference frame were drawn, after a quick and easy data post-processing using MATLAB. By visualizing the trajectory path, more than one family of solutions is distinguished. From figure 4.5 (on the left) it is evident that 2 families of solutions are present with a clear separation on departure date 29/10/2025 (case 3), having a first trajectory pointing upwards in the second quadrant and the other one pointing downwards

Departure	Duration $[days]$	Final Energy $[kg^2/s^2]$	Fuel consumed $[kg]$
15/10/2025	78.6	0.20	2.004
22/10/2025	90	0.07	1.810
22/10/2025	75.5	0.20	2.886
29/10/2025	80	0.02	6.572
29/10/2025	80.8	0.20	0.752
5/11/2025	75	0.18	1.670
5/11/2025	69	0.30	1.873

Table 4.5: Cases selected as local optimal for escape trajectories

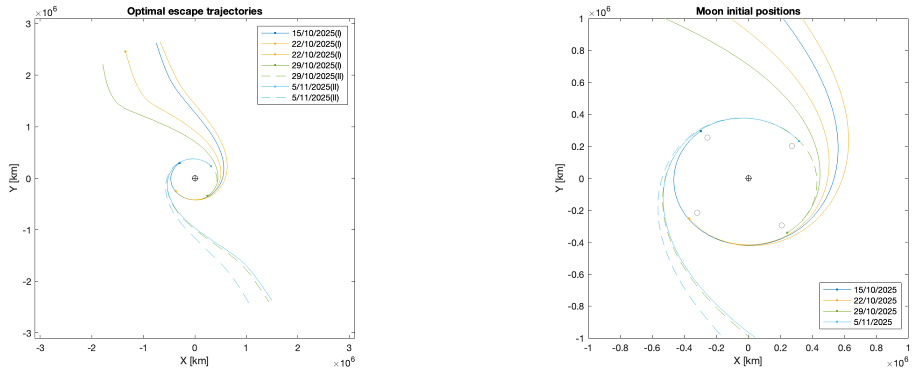

(a) (b)

Figure 4.5: Optimal Escape trajectories and detail of initial positions

in the fourth quadrant of graph. The optimum is found with departure date on 29^{th} October, duration 80.8 $days$ and final energy $c_3 = 0.2\,kg^2/s^2$ belonging to the second family, thus escaping Earth SOI in the fourth quadrant.

In the right hand of figure 4.5 there is a zoom-in of the previous image, in order to show relative positions of Moon, Earth and spacecraft at the initial point: as mentioned in section 4.1 starting dates are evenly separated through one period, following Moon revolution around Earth. Obviously three object are aligned, since EML2 is chosen as starting point.

4.3 Trajectory towards asteroid 2016 TB57

In the present study, mission target was chosen from a 75 asteroid shortlist, useful in this first part of the mission definition to offload operational overhead during compiling. The database is the same used by European Space Agency (ESA) mission analysts, during phase 0 of the mission called M-ARGO (Miniaturised Asteroid Remote Geophysical Observers). M-ARGO is a scientific mission aiming to bring a 12-U CubeSat to randezvous with multiple small and unknown Near Earth Asteroids (NEA) in order to measure size and weight and analyze their surface, collecting useful data for the scientific community.

Initially over 700 thousand small, spinning asteroids were screened by the mission analysis team, subsequently the above mentioned short-list was set, considering only reachable targets given electric propulsion capabilities and the pre-selected launch window between 2024 and 2025. A further objective is to reduce the choice to few target, taking into account differences in size, spin rate, distance from Earth and amount of fuel required to reach them [7].

4.3.1 Global evaluation

As far as this thesis is concerned, asteroid 2016 TB57 has been chosen from the shortlist, as test case for the mission of our concern; a single phase mission is considered by the code and duration of the maneuver is fixed at 3 years. The procedure connecting escape with interplanetary trajectory was fairly straightforward: the code uses as input the previously calculated position at the end of escape maneuver, expressed in heliocentric coordinates, and gives as outputs, among other data, the final mass of the satellite. Results are summarized with the help of a histogram which displays the amount of fuel used for the maneuver.

Looking at the results, it is immediately noticed that departure times with the lowest amount of fuel required aren't the same of the escape trajectory, and that's obviously because these trajectories also depends on the orbital parameter of the asteroid chosen as target of the mission. Thus, spacecraft position and velocity at the end of optimal escape maneuver could not be so convenient in order to reach the selected target for interplanetary trajectory. As before, a new analysis is done

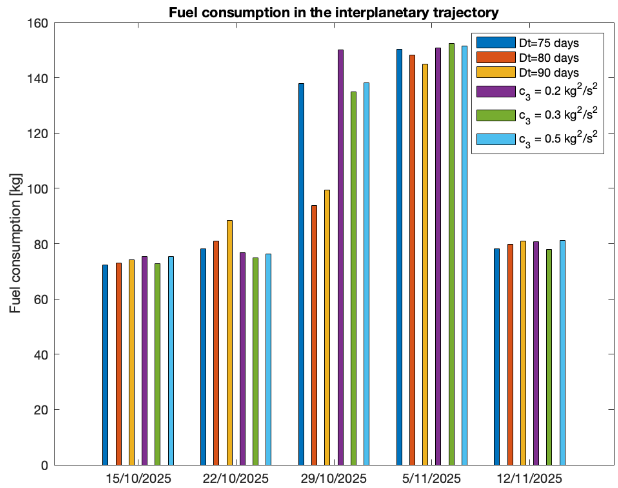

Figure 4.6: Graphical display of the amount of fuel consumed in the interplanetary maneuver to Asteroid 2016 TB57.

considering the most convenient combinations in term of mission duration and final energy c_3 at the end of escape maneuver. Cases are listed in table 4.6 where case with departure on 12 November wasn't considered because relative position among the spacecraft, Moon and Earth is approximately the same if compared with 15^{th} October, just after one synodic period.

Departure	Duration $[days]$	c_3 after escape $[kg^2/s^2]$	Fuel consumed $[kg]$
15/10/2025	75	0.35	72.178
22/10/2025	71.5	0.30	74.806
29/10/2025	80	0.02	93.685
5/11/2025	90	0.098	144.845

Table 4.6: Case selected as optimal for interplanetary trajectories

The amount of fuel required has a local minimum in case 1 (departure on 15/10/2025) leading to think that optimization can be reached around this date. It's noteworthy that an additional date was investigated (18^{th} October) but the optimization technique brought a higher fuel consumption. This means that the sought minimum could be on a prior date; this possibility was not investigated in this study but could be worth studying in the future.

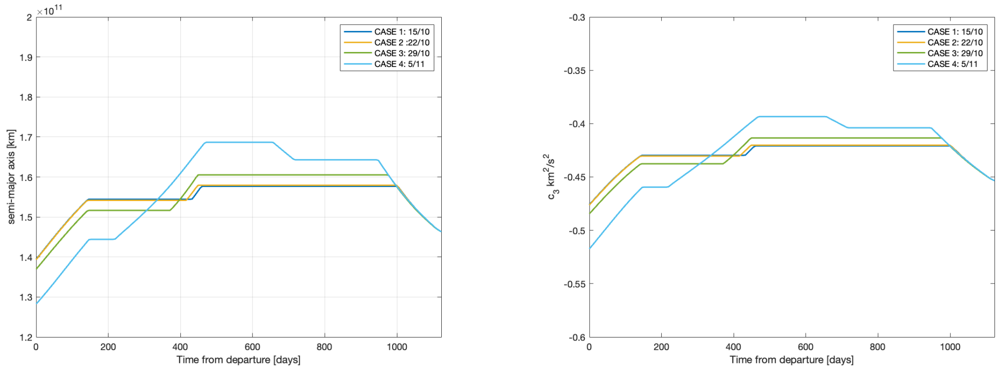

(a) (b)

Figure 4.7: Semi-major axis variation during time for interplanetary trajectories, compared with c_3 development

To better understand and review the results provided by the optimization method, a graphical display of orbital parameters during time have been deemed as appropriate. Looking specifically at semi-major axis, compared with the final energy c_3 during time, the same structure is clearly visible. Constant (or almost constant) lines representative of coasting arcs (with thrusters in off-mode), are joint through ramps which are the parts of the trajectory where the propulsion system is active, thus when a variation in orbital parameters occurs.

Right after escape, there is a first long thrust which brings the spacecraft to reach an elliptic orbit with a greater energy; one (cases 1,2 and 3) or two (case 4) adjustments are subsequently made in order to intersect the target orbit; then another long burn, represented with a negative slope, substantially brakes the spacecraft until the insertion in the target orbit. As mentioned before, this structure is essentially the same for every trajectory considered; furthermore, a parallelism between energy and semi-major axis developments is justified by the direct relation between energy, velocity and semi-major axis $\left(c_3 = -\frac{\mu}{2a}\right)$. Should be noted that the trajectories having the minimum request of fuel, are the one where the path from initial energy (or semi-major axis) to the final energy is the most direct, without waste of fuel. Furthermore, the best case is also the one with the greatest energy after escape, a crucial condition when the target is far from Earth. Case 1 and 2 (blue and yellow lines) are substantially overlapped, but with a closer look yellow line is slightly above the blue one, leading to a consequently higher use of fuel due to the longer breaking burn.

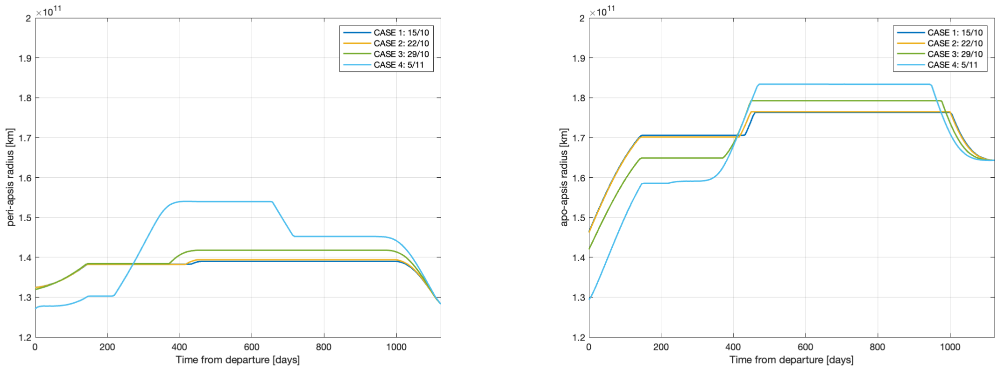

(a) (b)

Figure 4.8: Peri-apsis (a) and apo-apsis (b) development during interplanetary trajectories

In figure 4.8 peri-apsis (a) and apo-apsis (b) are depicted: the same structure is present, validating the logic explained before.

Further data about starting points of interplanetary trajectories could be helpful to better analyze the situation, position and velocity component in heliocentric reference frame at the end of the escape are summed up in table 4.7. Data in the

Case	Position			Velocity		
	r [A.U.]	θ [deg]	φ [deg]	u [km/s]	v [km/s]	w [km/s]
1	1.0034	97.439	0.046868	0.66917	30.388	-0.0072972
2	1.0033	100.93	0.039992	0.67099	30.38	-0.012778
3	1.0036	117.09	-0.00045837	0.73479	30.128	-0.022726
4	0.96566	134.26	0.013465	-0.27164	30.32	0.028534

Table 4.7: Position and velocity components in heliocentric reference frame at the end of escape

previous table confirm the position of the spacecraft in Earth proximity: $r \simeq 1\,\mathrm{AU}$ while right ascension θ and eastward component of the velocity v are concordant with Earth motion on its orbit around the Sun. Orbital parameters at the beginning of the interplanetary maneuver are listed in table 4.8.

From the values below we can conclude that the spacecraft enters an elliptic orbit having a much greater Semimajor Axis, if compared with mean values for the asteroid belt, between $3.1416 \cdot 10^8$ km and $5.3855 \cdot 10^8$ km (2.1 and 3.6 AU). The trajectory intersects asteroid 2016 TB57 orbit and the spacecraft performs a maneuver which results to be faster, optimizing also the duration of the mission.

Case	Semimajor axis [km]	Periapsis radius [km]	Apoapsis radius [km]	Inclination [deg]	Eccentricity
1	$1.3943 \cdot 10^{11}$	$1.3246 \cdot 10^{11}$	$1.464 \cdot 10^{11}$	2.796	0.05
2	$1.3932 \cdot 10^{11}$	$1.3242 \cdot 10^{11}$	$1.4621 \cdot 10^{11}$	2.6757	0.0495
3	$1.3696 \cdot 10^{11}$	$1.3192 \cdot 10^{11}$	$1.42 \cdot 10^{11}$	2.4752	0.0368
4	$1.2825 \cdot 10^{11}$	$1.271 \cdot 10^{11}$	$1.294 \cdot 10^{11}$	3.1856	0.009

Table 4.8: Orbital parameters at the end of escape.

4.3.2 Optimal interplanetary trajectory

By extracting the most convenient trajectory, a further graphical display can be considered: comparison between energy and Switching Function (SF) sign over time. Both the curves are represented in figure 4.9; the overlapping proves once again that SF (red curve) is high, thus propulsion is on exactly where an increasing in energy is depicted, while where there are horizontal lines, SF is low, meaning for the control that thrust isn't active.

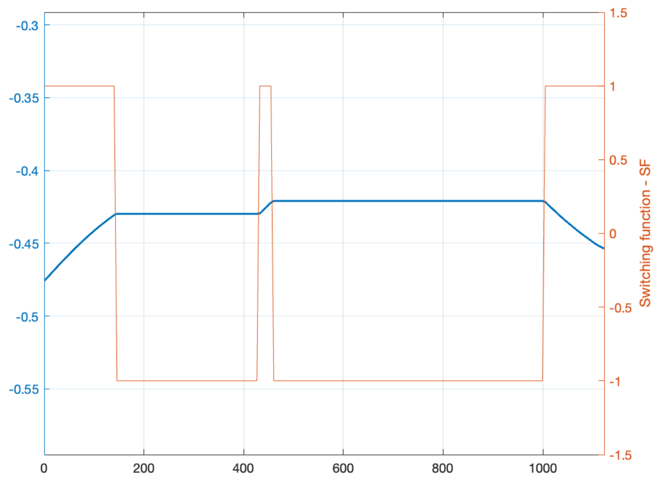

Figure 4.9: Energy and switching function comparison during time

Chapter 5

Conclusions

This thesis aims to study the use of an indirect method, exploited for missions towards Near Earth Asteroids (NEA), starting from Lagrangian points. Specifically, a mission towards asteroid 2016 TB57 departing from Earth-Moon Lagrangian Point 2 (EML2) was considered. Trajectory was divided into 2 parts: escape from Earth SOI (Geocentric phase) and interplanetary phase (Heliocentric).

The study is intended as a test-case, thus evaluates the feasibility of the maneuver in the wider context of mission analysis for a possible scientific mission towards NEA, such as M-ARGO by ESA. The optimization method takes into account perturbing accelerations on the spacecraft due to Earth oblateness, gravitational forces applied by Sun and Moon and Solar Radiation Pressure (SRP); four departure dates were considered throughout a month: a period of revolution of the Moon around Earth.

Starting with imposed switching structure (i.e. number of phases and burns during the trajectory), an optimal solution was obtained by integrating and solving the boundary value problem. Switching Function (SF) sign is checked at the end and switching structure is eventually modified in case it doesn't match with the one settled at the beginning. Algorithm proved to be relatively fast and reliable, however the outcome of integration procedure is strongly dependent on initial solution. In some cases, when external constraints were too far from the initial guess, convergence didn't occur, thus some adjustments on the above mentioned constraints had to be done, forcing the user to proceed with small steps towards the actually result sought.

Once optimum for escape maneuver was found, the algorithm optimizing interplanetary trajectories proved to be highly reliable and faster than before. In this case constraints weren't changed and starting position and velocity came from solution of the previous analysis.

Escape maneuver analysis highlighted that fuel consumption depends on departure date (other than imposed constraints), which is strictly connected with relative position between the Sun and the spacecraft. In fact perturbing gravitational force of the Sun could affect the trajectories whether in a favourable or unfavourable way depending on the direction of application.

Plotting the best trajectories found on equatorial plane (Geocentric reference frame), the presence of two different trajectory families is clear: the first family escape earth SOI in the second quadrant, the second one in the fourth quadrant. Optimal trajectory found in this study belongs to the second family.

As far as interplanetary trajectories are concerned, optimum was found with different departure date and different combination of constraints. A rising fuel consumption was registered throughout the month, placing the optimum on the first date considered.

Considering orbital parameter values, it is understood that the spacecraft enters a high energy elliptic orbit in order to reach the asteroid belt in a short period, but it is forced to a break (burn in direction opposite to velocity) in order to enter an orbit around the selected target. By analysing orbital parameter variations during interplanetary trajectories, was found that smaller variation in orbital energy lead to smaller amount of fuel consumed.

Further studies about this topic certainly need to be done: first of all, analysis of trajectories towards other possible asteroids is necessary in order to pick the most convenient target to reach for the mission; in second place some improvements in terms of dynamic model could lead to more precise results, useful in the following steps of mission analysis: all perturbing forces should be considered and starting point should be set in orbit around EML2 (for example on a Halo orbit or Lissajous orbit). Furthermore, the interplanetary trajectory under the influence of the target asteroid should be considered and add to the heliocentric arc analyzed in this thesis.

Bibliography

[1] Roger R Bate. *Fundamentals of astrodynamics / Roger R. Bate, Donald D. Mueller, Jerry E. White*. eng. 2nd ed. Dover books on astronomy. New York: Dover, 1971. ISBN: 9780486600611.

[2] Ales Bezdek and Josef Sebera. "Matlab script for 3D visualizing geodata on a rotating globe". In: *Computers Geosciences* 56 (July 2013), pp. 127–130. DOI: 10.1016/j.cageo.2013.03.007.

[3] Arthur E Bryson and Yu-Chi Ho. *Applied optimal control: optimization, estimation, and control*. Routledge, 2018.

[4] Lorenzo Casalino, Guido Colasurdo, and Dario Pastrone. "Optimal low-thrust escape trajectories using gravity assist". In: *Journal of Guidance, Control, and Dynamics* 22.5 (1999), pp. 637–642.

[5] J.W. Cornelisse, H.F.R. Schöyer, and K.F. Wakker. *Rocket Propulsion and Spaceflight Dynamics*. Aerospace Engineering Series. Pitman, 1979. ISBN: 9780273011415.

[6] *Earth Gravitational Model 2008 (EGM2008)*. 2022. URL: https://earth-info.nga.mil/.

[7] *M-Argo: Journey of a suitcase-sized asteroid explorer*. 2021. URL: https://www.esa.int/Enabling_Support/Space_Engineering_Technology/Shaping_the_Future/M-Argo_Journey_of_a_suitcase-sized_asteroid_explorer.

[8] Claudio Maccone. "Optimal Trajectories from the Earth-Moon L1 and L3 Points to Deflect Hazardous Asteroids and Comets". In: *Annals NY Academy of Science* 1017 (Dec. 2006), pp. 370–385. DOI: 10.1196/annals.1311.020.

[9] Luigi Mascolo and Lorenzo Casalino. "Escape Trajectories from Lagrangian Points with Electric Propulsion". In: ().

[10] *Missions to Asteroids*. 2022. URL: https://nssdc.gsfc.nasa.gov/planetary/planets/asteroidpage.html.

[11] Francesco Simeoni et al. "Indirect optimization of satellite deployment into a highly elliptic orbit". In: *International Journal of Aerospace Engineering* 2012 (2012).

[12] *Sun, Earth and Moon Position 3D Simulator*. 2022. URL: https://en.tutiempo.net/astronomy/sun-earth-moon-3d.html#UTC20220322T1725.

[13] Euaggelos E. Zotos, Angela Perdiou, and Vassilis Kalantonis. "Numerical investigation for the dynamics of the planar circular Pluto-Charon system". In: *Planetary and Space Science* 179 (2019), p. 104718. ISSN: 0032-0633. DOI: https://doi.org/10.1016/j.pss.2019.104718. URL: https://www.sciencedirect.com/science/article/pii/S0032063318303234.

Acknowledgments

At the end of this journey, I would like to thank my tutor, professor Casalino Lorenzo, for the opportunity he offered me. I had the chance to apply my knowledge and I learnt to be more autonomous in my work.

A heartfelt thank you goes to my family and my friends who've constantly supported me and my colleagues, with whom I managed to overcome every challenge throughout the entire university experience.